Molecular Cancer Therapeutics

Acridine Derivatives as Inhibitors of the IRE1α–XBP1 Pathway Are Cytotoxic to Human Multiple Myeloma

Dadi Jiang[1], Arvin B. Tam[2], Muthuraman Alagappan[1], Michael P. Hay[3], Aparna Gupta[1], Margaret M. Kozak[1], David E. Solow-Cordero[4], Pek Y. Lum[5], Nicholas C. Denko[6], Amato J. Giaccia[1], Quynh-Thu Le[1], Maho Niwa[2], and Albert C. Koong[1]

Abstract

Using a luciferase reporter–based high-throughput chemical library screen and topological data analysis, we identified *N*-acridine-9-yl-*N*',*N*'-dimethylpropane-1,3-diamine (DAPA) as an inhibitor of the inositol requiring kinase 1α (IRE1α)–X-box binding protein-1 (XBP1) pathway of the unfolded protein response. We designed a collection of analogues based on the structure of DAPA to explore structure–activity relationships and identified N^9-(3-(dimethylamino)propyl)-N^3,N^3,N^6,N^6-tetramethylacridine-3,6,9-triamine (3,6-DMAD), with 3,6-dimethylamino substitution on the chromophore, as a potent inhibitor. 3,6-DMAD inhibited both IRE1α oligomerization and *in vitro* endoribonuclease (RNase) activity, whereas the other analogues only blocked IRE1α oligomerization. Consistent with the inhibition of IRE1α-mediated *XBP1* splicing, which is critical for multiple myeloma cell survival, these analogues were cytotoxic to multiple myeloma cell lines. Furthermore, 3,6-DMAD inhibited *XBP1* splicing *in vivo* and the growth of multiple myeloma tumor xenografts. Our study not only confirmed the utilization of topological data analysis in drug discovery but also identified a class of compounds with a unique mechanism of action as potent IRE1α–XBP1 inhibitors in the treatment of multiple myeloma. *Mol Cancer Ther; 15(9); 2055–65. ©2016 AACR.*

Introduction

The endoplasmic reticulum (ER) is the central organelle where newly synthesized proteins mature and are properly folded. A variety of stresses, including glucose deprivation, hypoxia, and chemotherapeutic treatment, cause accumulation of unfolded or misfolded proteins inside the ER, resulting in ER stress. In response to ER stress, the cell initiates the unfolded protein response (UPR) to restore protein folding homeostasis. The UPR actively reduces protein translation, increases expression of ER chaperones and protein-folding enzymes, and clears misfolded proteins for degradation (1). However, under prolonged ER stress, the UPR paradoxically also induces cell death by apoptosis (2).

In mammalian cells, the UPR consists of three primary signaling pathways, each of which includes an ER membrane-bound sensor protein that activates a b-ZIP (Basic Leucine Zipper domain) transcription factor. The three pathways are (i) inositol requiring kinase 1α (IRE1α) and X-box binding protein-1 (XBP1); (ii) protein kinase RNA-like ER kinase (PERK) and activating transcription factor 4 (ATF4); and (iii) activating transcription factor 6 (ATF6), which serves as both a sensor and transcriptional factor (1). The IRE1α–XBP1 branch is involved in lipid synthesis, ER-associated protein degradation (ERAD), protein folding, translocation to ER, and secretion (1). At the molecular level, IRE1α is a type I transmembrane protein consisting of a serine/threonine kinase domain and an RNase domain. In the presence of ER stress, IRE1α dimerizes and oligomerizes while stimulating trans-autophosphorylation, activating the RNase domain (3, 4). Activated IRE1α RNase excises a 26-nucleotide intron from the human *XBP1* mRNA and causes a translational frame shift, generating the spliced and activated form of XBP1 (XBP1s; Fig. 1A; refs. 1, 5). In addition to its *XBP1* splicing activity, activated IRE1α also preferentially degrades ER-associated mRNAs, a process known as regulated IRE1-dependent decay (RIDD; refs. 6, 7).

Studies in animal models have revealed that the UPR is implicated in various types of human cancer and targeting key components of the UPR has emerged as a promising therapeutic strategy (5). The IRE1α–XBP1 pathway plays an indispensable role in tumor growth, metastatic progression, and chemoresistance (8, 9). Expression and activation of XBP1 has been correlated with poor clinical outcome in breast cancer (10, 11) and angiogenesis in pancreatic cancer (12). As a mediator of survival, XBP1 has been extensively characterized

[1]Department of Radiation Oncology, Stanford University, Stanford, California. [2]Department of Biological Sciences, University of California, San Diego, San Diego, California. [3]Auckland Cancer Society Research Centre, Faculty of Medical and Health Sciences, The University of Auckland, Auckland, New Zealand. [4]High-Throughput Bioscience Center, Department of Chemical and Systems Biology, Stanford University, Stanford, California. [5]Ayasdi Inc., Menlo Park, California. [6]Department of Radiation Oncology, Ohio State University, Columbus, Ohio.

Note: Supplementary data for this article are available at Molecular Cancer Therapeutics Online (http://mct.aacrjournals.org/).

Current address for P.Y. Lum: Capella Bio, Palo Alto, California.

Corresponding Author: Albert C. Koong, Stanford School of Medicine, 269 Campus Drive, CCSR-1245C, Stanford, CA 94305. Phone: 650-498-7703; Fax: 650-723-7381; E-mail: akoong@stanford.edu

doi: 10.1158/1535-7163.MCT-15-1023

in multiple myeloma, a plasma cell malignancy (13, 14). XBP1 is indispensable for plasma cell differentiation (15) and its expression is elevated in human multiple myeloma cells (16). XBP1 expression knockdown severely compromised RPMI 8226 multiple myeloma cell growth *in vitro* (17) and sensitized mouse myeloma cells for stress-induced apoptosis (18). Conversely, Eμ-myc–driven XBP1s expression promoted multiple myeloma pathogenesis in mice (14). Consistent with these results, XBP1s expression is associated with poor multiple myeloma patient survival (13, 19).

Several groups have identified small molecule inhibitors that selectively block IRE1α–XBP1 activation (5, 20), including those targeting the RNase domain [STF-083010 (21), salicylaldehydes (22), 4μ8C (23), MKC-3946 (17), and toyocamycin (24)] and directly interfering with ATP binding ("Compound 3"; ref. 25). Other members of the hydroxy–aryl–aldehydes (HAA) class, to which 4μ8C and MKC-3946 belong, were also extensively tested (26, 27). Given the complexity of the UPR, and the therapeutic potential of small molecule inhibitors targeting this pathway, combining conventional drug screening data with novel quantitative analysis may accelerate the drug development process.

To this end, we applied topological data analysis (TDA) to assist cell-based high-throughput screen (HTS). TDA is based on a branch of mathematics characterizing the geometric property of shapes with mathematical algorithms (28) and is a topologic framework of many machine-learning algorithms that quantify the shape of a large, but finite, number of data points. TDA has significant advantages over traditional hierarchical clustering in analyzing complex drug screening data. In contrast to hierarchical clustering that makes irreversible sequential choices about similarity and begins to lose utility when data grow in size, TDA maintains each data point individually throughout the process and performs extremely well in high-dimensional, large volume data and maintains its visual representations (29). Describing the results of an HTS is a multidimensional, complex signal challenge and TDA is particularly well suited to separate the signal from the background. To date, TDA has been applied to data analysis in cancer (29, 30), diabetes (31), neurological disorder (32), viral evolution (33), and the immune system (34).

Using an HTS combined with TDA, we identified a cluster of acridine analogues as specific inhibitors of the IRE1α–XBP1 axis that are cytotoxic to multiple myeloma cell lines. We also revealed a previously unidentified mechanism of action (MOA) for any existing inhibitor of IRE1α. Therefore, this study provides mechanistic insight of the biology of IRE1α activation and demonstrates the potential for targeting this MOA for therapeutic gain.

Materials and Methods

Compounds

For the chemical library screen, 113,500 compounds from the ChemDiv, SPECS, and Chembridge libraries were screened at the Stanford University High-Throughput Bioscience Center (HTBC; ref. 21). The detailed specifications and criteria for compound selection can be found at the HTBC website (http://htbc.stanford.edu/compounds.html). Individual screening compounds for the confirmation assay were ordered from ChemDiv. Acridine derivatives were synthesized or obtained from the compound library at Auckland Cancer Society Research Centre at University of Auckland. These compounds are further characterized in Supplementary Material. Thapsigargin (Tg) was obtained from Sigma Aldrich.

Cell culture

HT1080 and HEK293 cells overexpressing IRE1α-GFP were maintained in DMEM. RPMI 8226 and MM1.R cells were maintained in RPMI1640 medium. All media were supplemented with 10% FCS and 1% penicillin–streptomycin and cells were cultured at 37°C with 5% CO_2. Cell lines were authenticated using short tandem repeat analysis at ATCC and used within 6 months' culturing. The cells were obtained in 2001 (HT1080), 2009 (RPMI8226 and MM1.R), and 2011 (HEK293).

Topological data analysis

Analysis was performed using Iris software (Ayasdi Inc.). The description of the implementation of TDA in the software is described in ref. 29.

Western blotting

Western blotting was performed according to standard protocols. Antibodies used include: anti-XBP1s (1:1,000; BioLegend), anti-XBP1 (1:1,000; Abcam), anti-IRE1α, anti-phospho-eIF2α, anti-phospho-eIF2 (1:1,000; Cell Signaling Technology) and anti-β-actin (1:1,000; Santa Cruz Biotechnology).

Cell viability assay

For cell viability assay, 2×10^4 cells per well were plated into 96-well plates and treatment started 0 to 12 hours after plating. After 24 hours of treatment, XTT reagent (ATCC) was added to the wells. Then cells were incubated for 2 hours and absorbance was measured at both 475 and 660 nm using a BioTek Synergy H1 plate reader.

In vitro nuclease assay and kinetic analysis

In vitro nuclease assays were performed as described in ref. 35. Reactions were performed in nuclease reaction buffer (40 mmol/L HEPES 7.0, 10 mmol/L $Mg(OAc)_2$, 50 mmol/L KOAc, 5 mmol/L DTT) at 30°C for the indicated amount of time, with 2 mmol/L ADP, 1 μmol/L recombinant human IRE1α (hIRE1α), and labeled RNA at 0.15 nmol/L (10 fmol/reaction). Upon incubation for 30 minutes, reactions were stopped and RNA was extracted using phenol/chloroform, ethanol precipitated, analyzed on a denaturing 6% urea acrylamide gel and visualized by autoradiography.

IRE1α oligomerization assay

IRE1α oligomerization assay was performed as described previously (36). Briefly, reactions were set up using the same nuclease reaction buffer, 2 μmol/L recombinant hIRE1α, 2 mmol/L ADP, and 60 μmol/L of the indicated compound. All reactions were performed in 20 μL with 10% DMSO to account for vehicle and incubated for 15 minutes at 30°C to allow for oligomerization. The optical density of the sample was measured at 500 nm using a NanoDrop 2000 (Thermo Scientific).

IRE1α-GFP foci formation assay

To visualize IRE1α foci, HEK293 cells stably expressing doxycycline-inducible hIRE1α-GFP (37) were grown on a cover slip and IRE1α-GFP was induced with 10 nmol/L doxycycline 24 hours

before start of treatments. Cells were then pretreated with compound for 1 hour before addition of 300 nmol/L Tg for an additional 2 hours. For immunofluorescence, primary anti-GFP antibody (1:1,000; Roche) and Alexa Fluor 568 secondary antibody (1:2,000; Life Technologies) were used.

Bioluminescent imaging

Luciferase activity was measured noninvasively using the IVIS imaging system (PerkinElmer). Mice were injected intraperitoneally with 300 mg/kg luciferin (Biosynth) and anesthetized by 3% isoflurane (Butler-Schein). Exposure time was set as 1 second for ventral view. All images were analyzed using Living Image software version 4.2 (PerkinElmer). *In vivo* bioluminescent signal was quantified by taking the average photon count per second per square centimeter.

Murine multiple myeloma xenograft model

A total of 5×10^6 RPMI 8226 cells were implanted subcutaneously into the flanks of 4 to 6 weeks' old NOD SCID mice (Charles River Laboratories). Drug treatment started when the sizes of the tumors reached approximately 150 mm^3. Four tumor-bearing mice per group were treated with 10 mg/kg 3,6-DMAD or vehicle (saline) intraperitoneally once every 2 days. Tumor volume was measured as previously described (38).

Results

Identification of inhibitors of the IRE1α–XBP1 pathway through high-throughput chemical library screen and TDA

To identify inhibitors of XBP1 activation, we conducted a luciferase reporter-based high-throughput chemical library screen. In this reporter construct, firefly luciferase is fused in frame with the human *XBP1s* mRNA sequence, resulting in luciferase expression only when *XBP1* mRNA is spliced by activated IRE1α into the *XBP1s* form. This construct, as well as a CMV promoter-driven control construct to normalize for potential off-target effects, were stably introduced into the HT1080 human fibrosarcoma cell line (HT1080-XBP1-luc and HT1080-CMV-luc, respectively; Fig. 1A; ref. 39). Using the HT1080-XBP1-luc cell line, we performed the primary screen with 113,500 unique chemical compounds at a single concentration of 10 μmol/L (Fig. 1B). ER stress was induced by 300 nmol/L Tg, an ER Ca^{2+} ATPase inhibitor, and luciferase activity was measured 24 hours later (21). We then prioritized 990 compounds that displayed >40 %inhibition (compared with vehicle control) without nonspecific toxicity or nonspecific inhibition of luciferase activity for a secondary screen, in which all the compounds were assessed at eight concentrations ranging from 0.156 to 20 μmol/L in both types of reporter cell lines to determine dose-dependent activity (Fig. 1B).

To evaluate the results in a comprehensive manner, inhibition values of all 990 compounds were visualized in a heatmap generated by hierarchical clustering (Fig. 1C). The six subclusters represent different types of compound effects, including activation of XBP1-luc activity at higher doses (*I*), nondose-dependent inhibition (*II*), dose-dependent inhibition (*III* and *V*), and toxicity at higher doses (*IV* and *VI*). To evaluate more robustly the relationships between compounds and increase the accuracy of the hit selection, we analyzed the results of the secondary screen using TDA. An unbiased compound network was constructed by simultaneously considering the inhibition values across all the conditions for all the compounds (Fig. 1D). By quantitatively color-scaling the individual nodes (groups of compounds) in the network based on their inhibition values, we identified two regions that displayed selective inhibition of HT1080-XBP1-luc but not HT1080-CMV-luc activity, thus highlighting a set of compounds that specifically inhibit *XBP1* splicing with minimal nonspecific effects. Through more detailed analysis of the dose-inhibition curves for individual compounds in these regions, we identified four compounds with optimal curve fitting as well as magnitude of inhibition (Fig. 1D and E).

Interestingly, a previously identified IRE1α inhibitor through the same chemical library screen, STF083010, was also clustered in one of these regions, which served as an internal positive control for the validity of the TDA approach (21, 23). More significantly, the other compounds highlighted in these clusters would not necessarily be singled out as promising hits based upon conventional curve fitting–based selection criteria. To confirm the luciferase reporter-based assay results, we performed Western blotting to analyze the effect of these compounds on endogenous *XBP1* splicing in HT1080 cells induced by Tg. Of the top four candidate compounds, STF089106 displayed the most prominent inhibition on XBP1s protein expression without affecting expression of unspliced XBP1 (XBP1u; Fig. 1F, data not shown). Phospho-eIF2α levels were not attenuated by STF089106 treatment, suggesting that STF089106 specifically targeted the IRE1α–XBP1 branch instead of inhibiting the UPR in general. On the basis of these data, we selected STF089106 (1, *N*-acridine-9-yl-*N*',*N*'-dimethylpropane-1,3-diamine, DAPA; refs. 40, 41) for further analysis.

Acridines are DNA-binding agents and topoisomerase poisons (42) that have been previously identified as antitumor and antibacterial therapeutics (43). DAPA is an analogue of mAMSA, an anilinoacridine with activity against leukemia (44), and the acridine carboxamide (2, N-[2-(dimethylamino)ethyl]acridine-4-carboxamide, DACA). DACA has been tested in phase II trials against multiple types of cancers (45–48).

Validation of DAPA analogues as inhibitors of the IRE1α–XBP1 pathway

Upon identification of DAPA as a potential screening hit, we independently synthesized this molecule to confirm its activity (designated Compound 5) and designed a small set of analogues to explore the structure–activity relationships (SAR) of this compound (Fig. 2). 9-Aminoacridines bearing basic amine side chains have been characterized as DNA-affinic cytotoxins (49) and we sought to determine whether the SAR for inhibiting *XBP1* splicing is mapped to that required for DNA binding. DAPA contains a DNA intercalating 9-aminoacridine chromophore and we explored variations in the chromophore with analogues (Compound 5, 6, 10, and 11). Variations in side chain amine pK_a (acid dissociation constant) were explored with analogues Compound 5, 7, 8, and 9. We further analyzed the role of the side chain using a series of neutral analogues of varying lipophilicity with analogues Compound 1 to 3 (Fig. 2A).

We then compared the effect of these analogues (5 to 30 μmol/L) on endogenous UPR marker proteins in HT1080 cells treated with Tg. All compounds containing the entire acridine chromophore demonstrated inhibition of *XBP1*

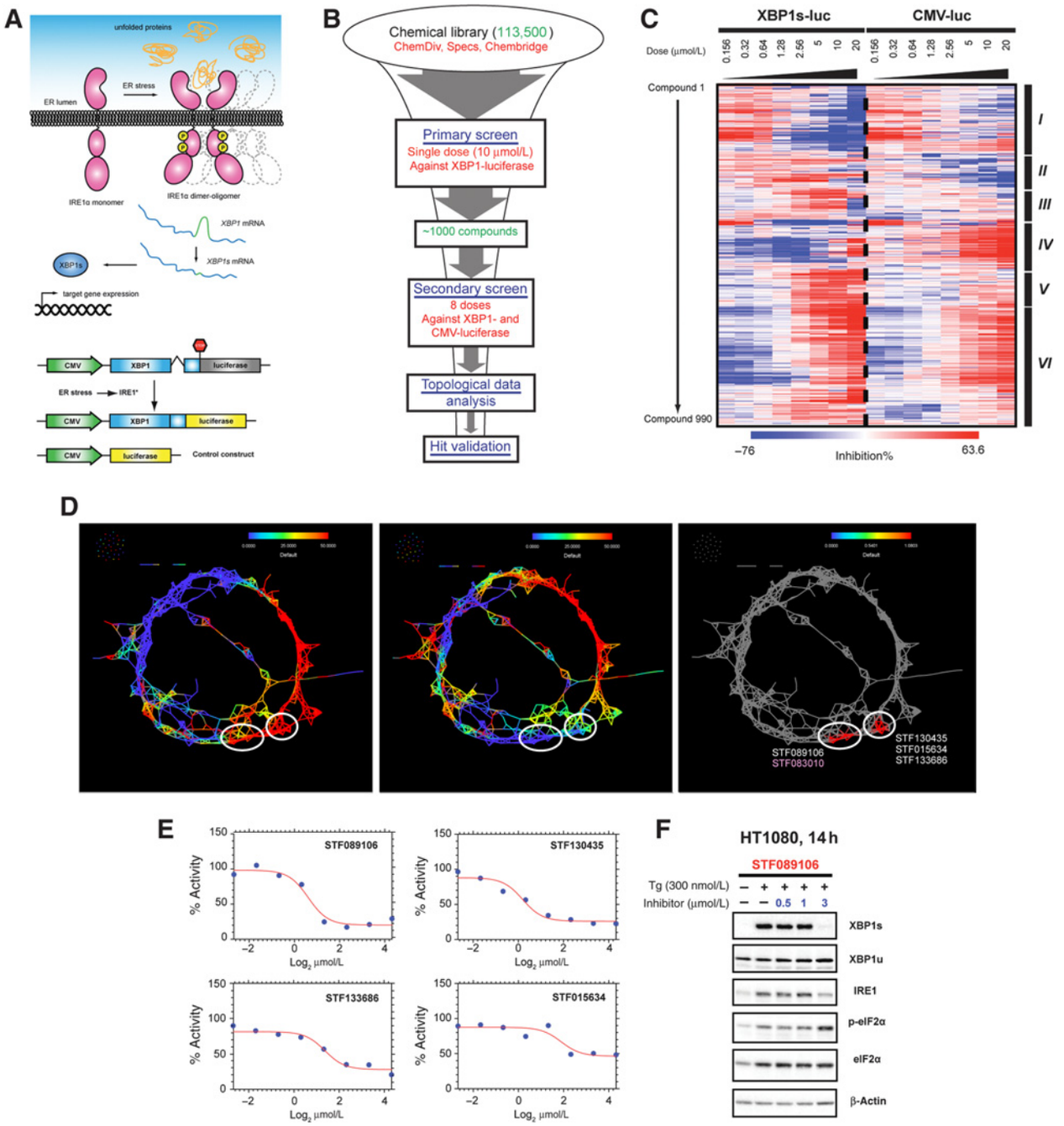

Figure 1.

Identification of small molecule inhibitors of the IRE1α–XBP1 pathway through HTS and TDA. **A,** top, schematic view of ER stress-induced IRE1α activation and *XBP1* mRNA splicing. Dashed lines show high-order assembly of IRE1α; bottom, schematic view of the luciferase reporter constructs used in the study. **B,** flow chart of the HTS. **C,** heatmap showing percentage of inhibition values for the 990 compounds selected in the secondary screen across the eight doses on both reporter cell lines. Red, positive percentage of inhibition. Blue, negative percentage of inhibition (higher levels of luciferase activity compared to vehicle control). **D,** TDA analysis of the secondary screen data. The three graphs are based on an Iris rendering of a Reeb graph of the screening data. Individual nodes represent compounds connected with edges based on the similarity in their percentage of inhibition profiles. Red, 50% and higher inhibition; blue color, 0% inhibition. Left, Iris network of the compounds colored by percentage of inhibition values from HT1080-XBP1-luc cells treated with 10 μmol/L of individual compounds. Middle, the same network colored by percentage of inhibition values from HT1080-CMV-luc cells treated with 10 μmol/L of individual compounds. Right, compounds within the selected regions. White ellipses define regions with candidate compounds that inhibit XBP1-luciferase but have minimal inhibition of CMV-luciferase. STF083010 is colored in pink. **E,** dose-inhibition curves of the four selected compounds from HT1080-XBP1-luc cells. **F,** Western blotting analysis of HT1080 cells untreated and treated with 300 nmol/L Tg and varying doses of STF089106 for 14 hours. A panel of UPR marker proteins was analyzed. β-Actin was used as a loading control.

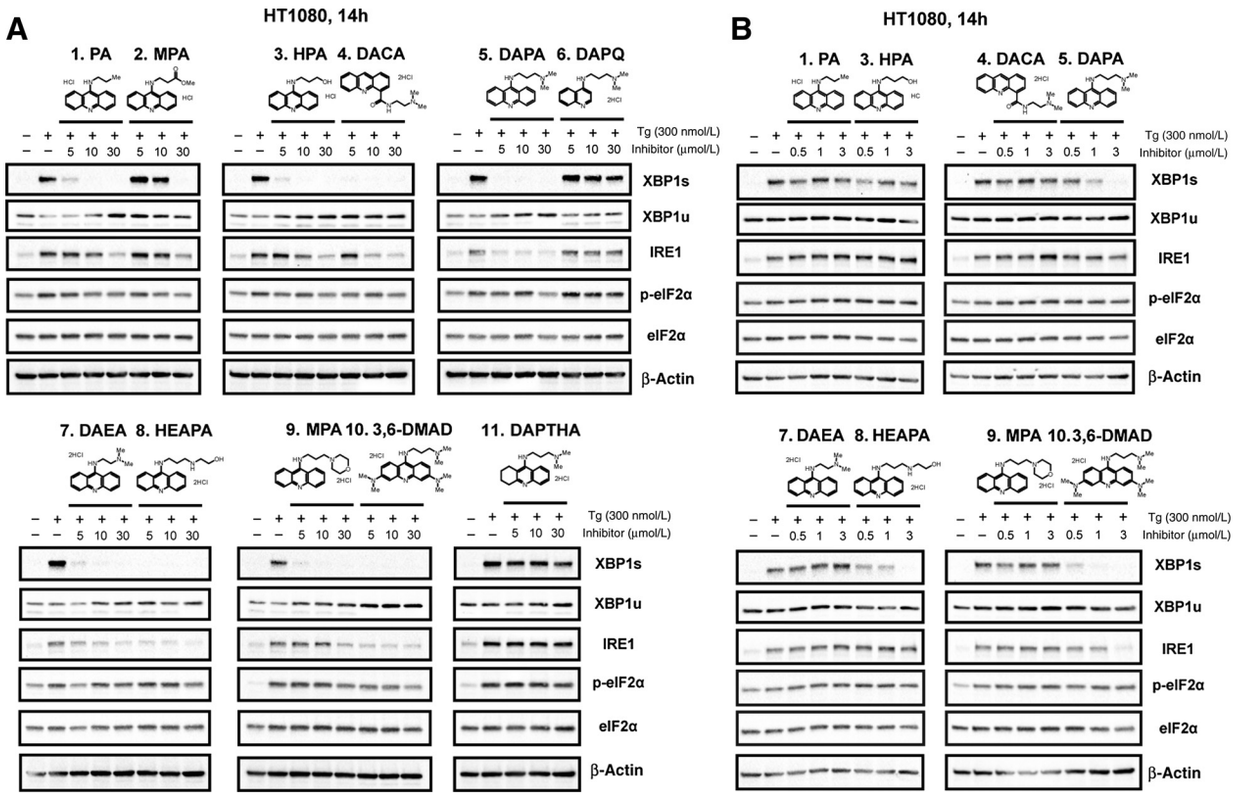

Figure 2.

Validation of acridine derivatives as inhibitors of the IRE1α–XBP1 pathway. **A,** Western blot analysis of a panel of UPR marker proteins in HT1080 cells untreated and treated with 300 nmol/L Tg plus 0 to 30 μmol/L of 11 acridine derivatives. β-Actin was used as a loading control. Chemical structures of the compounds are displayed on top of the blots. **B,** the same Western blot analysis with lower concentrations (0 to 3 μmol/L) for 8 of the 11 acridine derivatives that showed profound inhibition of XBP1s in **A**.

splicing, whereas saturation (Compound 11) or removal of one ring (Compound 6) resulted in loss of inhibition, suggesting that an acridine chromophore was important for inhibiting XBP1s. In contrast, phospho-eIF2α levels remained relatively unchanged, indicating that these compounds could preferentially block IRE1α–XBP1 with minimal impact on the other branches of UPR.

Next, we expanded our analysis of the more potent analogues (Compound 1, 3 to 5, 7 to 10) at lower concentrations (0.5 to 3 μmol/L; Fig. 2B). Both 9-aminoacridine (Compound 5) and acridine-4-carboxamide (Compound 4) displayed XBP1s inhibitory activity with the 9-aminoacridine demonstrating the greatest XBP1s inhibition at 1 μmol/L. Importantly, the 3,6-dimethylamino substitution on the acridine ring increased activity with Compound 10 showing XBP1s inhibition at as low as 0.5 μmol/L. These SAR data indicate that the acridine ring is critical for the activity of the drug to inhibit XBP1s. Variation in the basicity of the amine side chain was tolerated, although it appears that less basic amines, for example, Compound 9, were weaker inhibitors. A range of neutral substituents were also tolerated, albeit with reduced potency compared to Compound 5 (Fig. 2B). This targeted SAR dataset validated the activity of DAPA as an inhibitor of *XBP1* splicing and confirmed the utility of 9-aminoacridines as the basis for future drug development.

Mechanism of IRE1α–XBP1 inhibition by acridine derivatives

We explored the mechanism of inhibition of IRE1α–XBP1 by analyzing a selection of representative analogues, including Compound 10 (most potent), 5 (highly potent), 4 (limited potency), and 11 (inactive). To test whether inhibition occurs by directly disrupting the IRE1α–XBP1 interaction, we performed an *in vitro* IRE1α RNase assay with recombinant human IRE1α and ^{32}P-labeled human *XBP1* mRNA substrate (Fig. 3, top). Although Compound 10 blocked *in vitro XBP1* splicing almost completely at 10 μmol/L and Compound 11 was inactive as expected, Compounds 4 and 5 did not show activity in this assay, even at concentrations up to 500 μmol/L. Furthermore, we examined human *BLOS1* cleavage as an assay for RIDD. We determined that Compound 10 inhibited RIDD with similar efficacy as *XBP1* splicing (Fig. 3, bottom), suggesting that 3,6-dimethylamino substitution of the acridine ring is critical for global inhibition of IRE1α endonuclease activity. However, as both Compounds 4 and 5 displayed inhibitory activity against XBP1s in the cell-based assay, there could be an alternative mechanism by which these compounds interfere with IRE1α activity in intact cells that is not evident in the cell-free system.

Next, we determined the effect of these compounds on IRE1α dimerization and oligomerization, necessary for activation of its RNase activity. Initially, we performed an *in vitro*

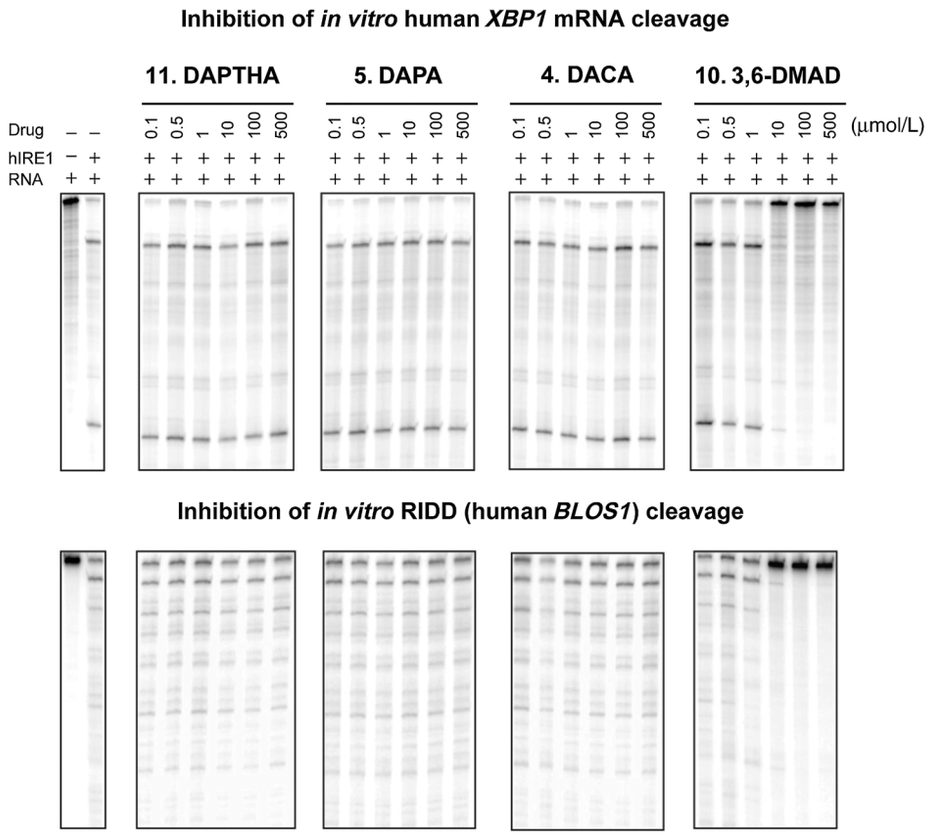

Figure 3.
In vitro IRE1α ribonuclease assay on a selection of acridine derivatives. Top, splicing of radiolabeled full-length human *XBP1* mRNA by recombinant hIRE1α (far left) and the effects of increasing doses of the four acridine derivatives on the splicing. Bottom, splicing of radiolabeled full-length human *BLOS1* mRNA by recombinant hIRE1α (far left) and the effects of increasing doses of the four acridine derivatives on the splicing.

IRE1α oligomerization assay, in which addition of ADP to purified IRE1α stimulates its oligomerization (Fig. 4A; ref. 36). Although treatment with each compound alone did not affect the optical readings, Compounds 4, 5, and 10 significantly attenuated ADP-induced IRE1α oligomerization. Interestingly, STF083010 did not show any activity in this assay, highlighting the unique mechanistic specificity of the acridine analogues on IRE1α oligomerization. The lack of inhibitory activity for Compound 11 demonstrates that an acridine ring is essential for inhibiting IRE1α activity by disrupting its oligomerization. In summary, the basic acridine ring in addition to an aminoalkyl side chain at the 4- or 9-position was sufficient for disrupting IRE1α oligomerization, but not adequate for inhibiting the established RNase activity. In contrast, the 3,6-dimethylamino substitution enabled both disruption of IRE1α oligomerization and inhibition of *XBP1* splicing activity.

To verify the results from the *in vitro* oligomerization assay in intact cells, we utilized HEK293 cells overexpressing GFP-tagged IRE1α in which IRE1α-GFP foci formation can be detected through fluorescence imaging after Tg treatment (Fig. 4B; ref. 37). We used immunofluorescence staining to detect IRE1α-GFP foci as higher concentrations of Compound 10 caused autofluorescence (Fig. 4C). We found that higher than 1 μmol/L of Compound 10 completely inhibited Tg-induced foci formation in living cells. These data are consistent with the *in vitro* oligomerization assay results and indicate that Compound 10 blocks XBP1 splicing by both inhibiting IRE1α RNase activity directly and disrupting IRE1α oligomerization.

9-Aminoacridine analogues display cytotoxicity against multiple myeloma cell lines *in vitro*

We performed XTT viability assays on both RPMI 8226 and MM1.R (dexamethasone-resistant) human multiple myeloma cells treated with selected analogues to characterize drug cytotoxicity. Consistent with their high potency in inhibiting XBP1s, Compounds 5 and 10 displayed significant cytotoxicity in these cells within the concentration range (0 to 6 μmol/L; Fig. 5A) and the weaker Compound 4 demonstrated only limited cytotoxicity (Fig. 5A). As a negative control, Compound 11, which was inactive in blocking XBP1s, failed to show any cytotoxicity on the multiple myeloma cells (Fig. 5A).

We also assessed the effect of these compounds on a panel of UPR marker proteins in multiple myeloma cells treated between 1 and 3 μmol/L and found a consistent correlation between the cytotoxicity of these compounds with the degree of inhibition of XBP1s (Fig. 5B). In summary, these findings demonstrate that 9-aminoacridines, particularly Compound 10, display cytotoxicity in multiple myeloma cells *in vitro*, which correlates with inhibition of the IRE1α–XBP1 pathway.

Potent inhibition of *XBP1* splicing by 3,6-DMAD *in vivo*

On the basis of the cell-based and cell-free assay results, we chose to evaluate the activity of 3,6-DMAD (Compound 10) *in vivo*. We utilized transgenic mice constitutively expressing the XBP1-luciferase reporter, which expresses luciferase activity under basal and inducible ER stress *in vivo* (39). After three intraperitoneal administrations of 3,6-DMAD at a dose of

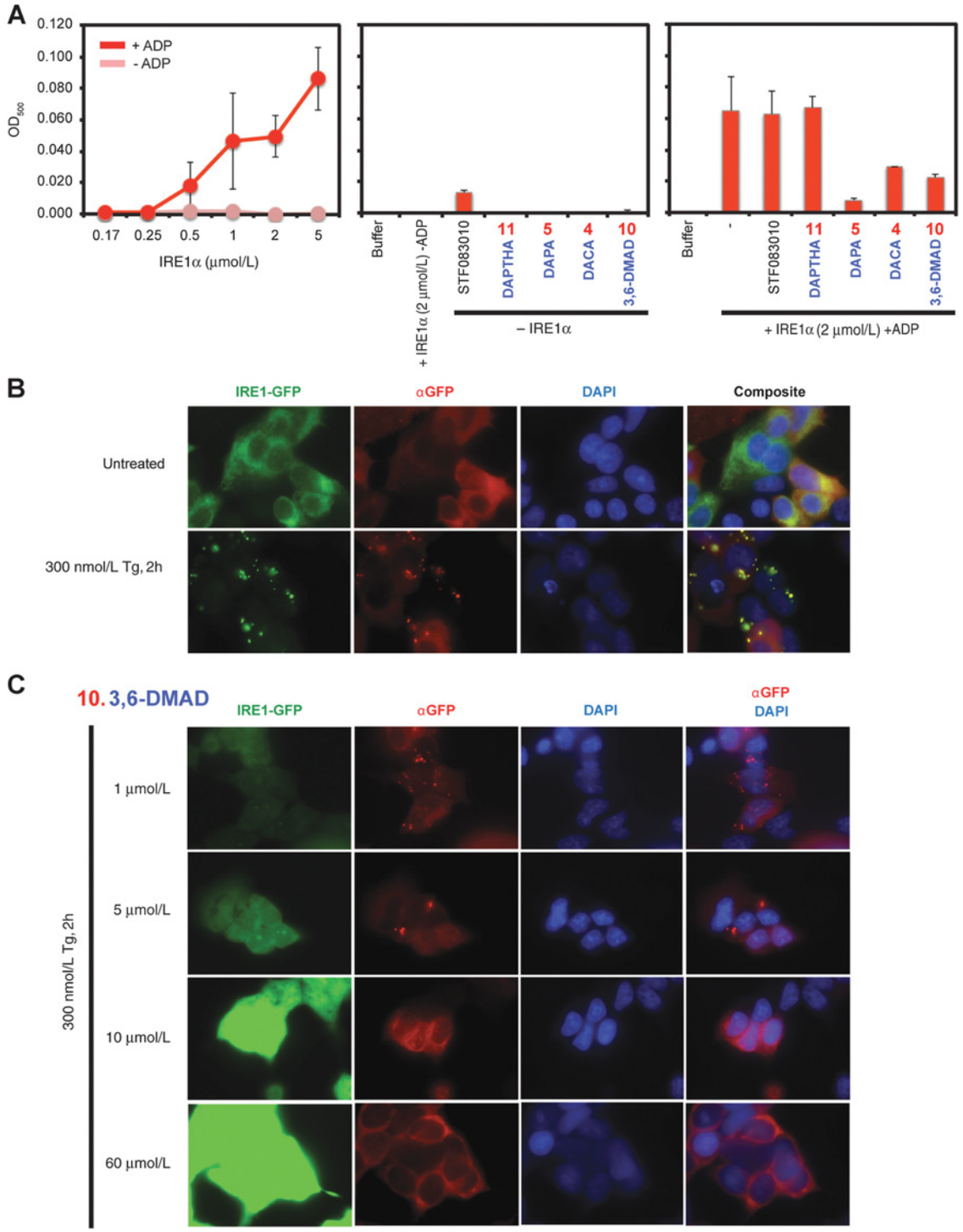

Figure 4.

In vitro IRE1α oligomerization and *in vivo* IRE1α-GFP foci formation assay. **A,** left, increasing concentration of recombinant IRE1α was used to perform *in vitro* oligomerization assays with or without 2 mmol/L ADP. Addition of ADP resulted in increased optical density (OD) at higher concentrations of IRE1α, indicating protein oligomerization. Middle, IRE1α without ADP or each acridine derivative alone do not significantly change optical density readings. STF083010 was used as a control. Right, reactions were performed with IRE1α plus ADP and 60 μmol/L of inhibitor. **B,** immunofluorescent imaging of HEK293 cells overexpressing an IRE1α-GFP fusion protein untreated and treated with 300 nmol/L Tg for 2 hours. IRE1α-GFP foci were detected both through GFP channel and immunofluorescently. DAPI staining was used to visualize nuclei. GFP/anti-GFP/DAPI channels are combined in the composite view on the right. **C,** the same immunofluorescent imaging as in **B** with 1 to 60 μmol/L of Compound 10 for 2 hours.

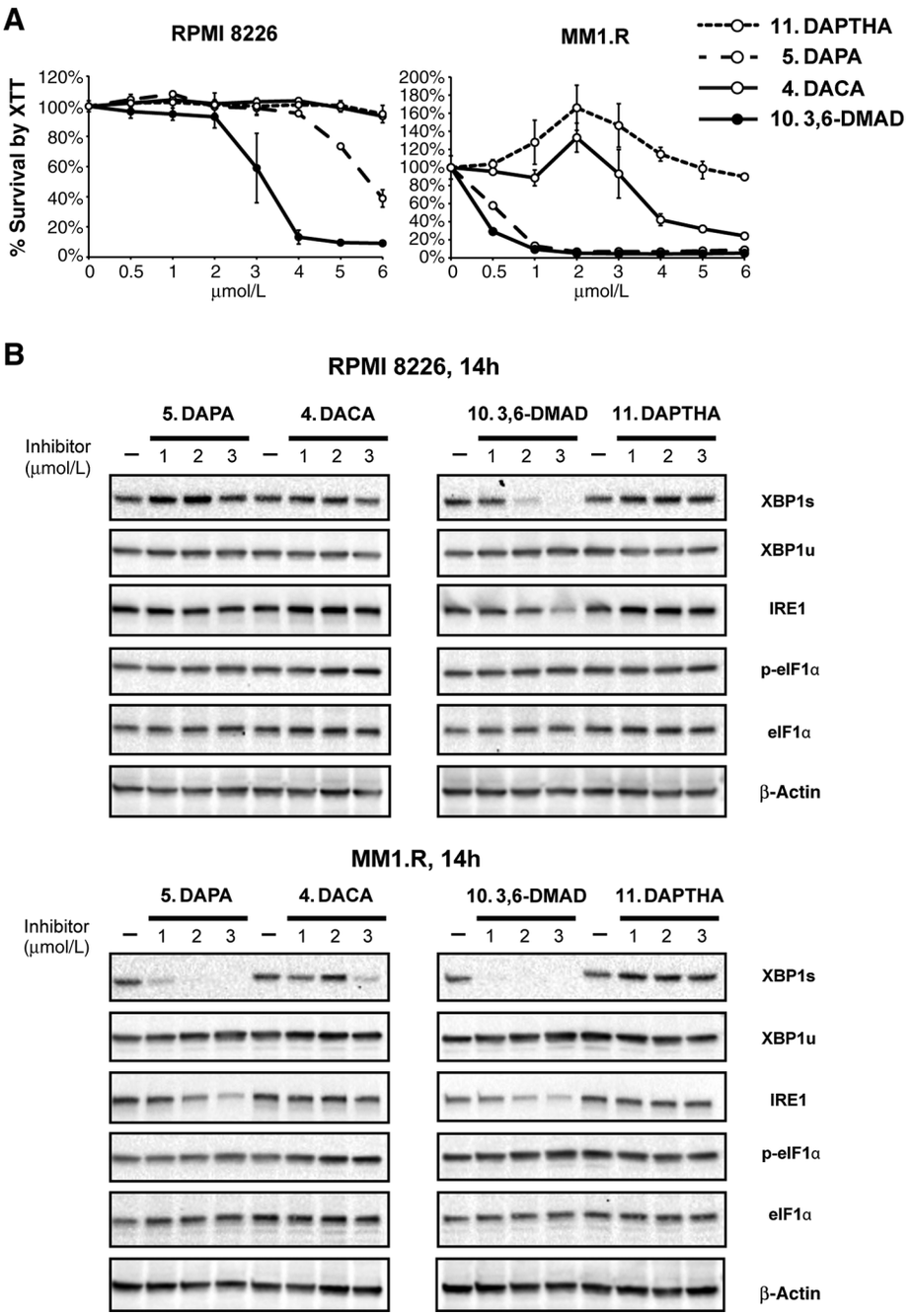

Figure 5.
Cytotoxicity of acridine derivatives on human MM cell lines. **A,** XTT cell viability assay of RPMI 8226 and MM1.R human MM cells treated with 0 to 6 μmol/L of Compound 4, 5, 10, and 11 for 24 hours. Background-subtracted optical absorbance values normalized to vehicle treatment (set to 100%) ± SD were plotted over the indicated compound doses. **B,** Western blot analysis of a panel of UPR marker proteins for both types of cells that were treated with 0 to 3 μmol/L Compound 4, 5, 10 and Compound 11 for 14 hours. β-Actin was used as a loading control.

10 mg/kg every 12 hours, this compound significantly inhibited *in vivo* luciferase activity assessed 3.5 days after the initial treatment (Fig. 6A), whereas treatment with vehicle did not cause any significant change (Fig. 6B).

3,6-DMAD suppresses multiple myeloma xenograft growth *in vivo*

To assess the effect of 3,6-DMAD on multiple myeloma tumor growth *in vivo*, we treated NOD SCID mice transplanted with RPMI 8226 cells subcutaneously with 10 mg/kg of 3,6-DMAD administered intraperitoneally every 48 hours. Compared with vehicle group, 3,6-DMAD-treatment significantly inhibited tumor xenograft growth (Fig. 6C and D).

Discussion

We previously performed a luciferase reporter–based HTS targeting the IRE1α–XBP1 pathway of the UPR. Using TDA on the HTS dataset, we identified DAPA as a potent inhibitor of *XBP1* splicing. We synthesized a set of DAPA analogues to explore the SAR and conclude that the acridine chromophore is critical for inhibition of *XBP1* splicing. Furthermore, a

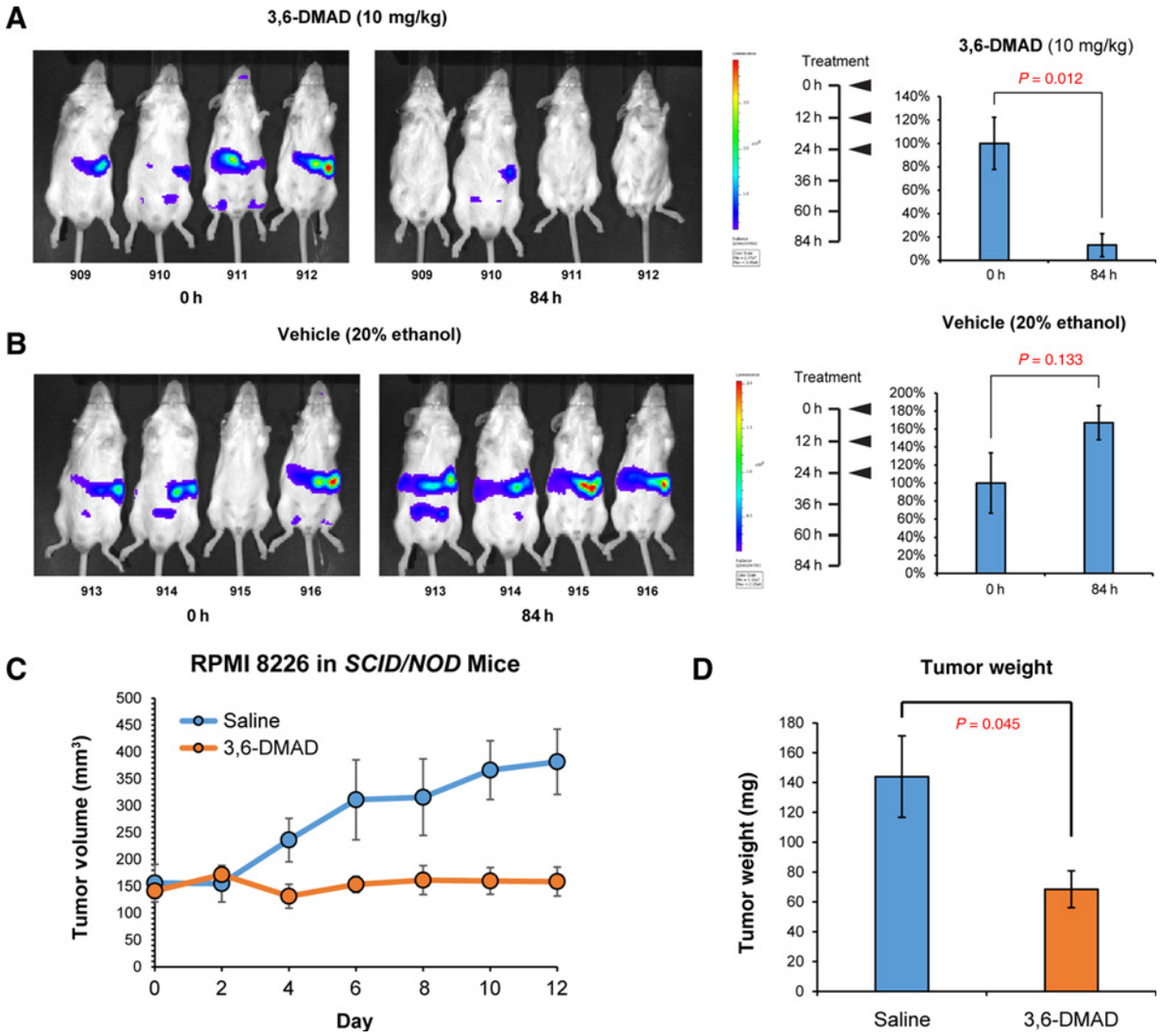

Figure 6.

In vivo inhibition of *XBP1* splicing and multiple myeloma xenograft growth by 3,6-DMAD. Bioluminescent images of mice expressing an XBP1-luciferase reporter gene treated with 3,6-DMAD (**A**) and vehicle (20% ethanol in saline; (**B**) after 84 hours. Treatment schedules and average luciferase activities normalized to 0 hour ± SD with the corresponding *P* values from Student *t* test are shown on the right. **C,** NOD SCID mice with subcutaneously implanted RPMI 8226 tumors were treated with 10 mg/kg 3,6-DMAD every 2 days or vehicle (saline). Tumor volumes were measured and plotted over time. **D,** upon euthanization of the tumor-bearing mice, tumors were dissected and tumor weights were measured and average weights ± SD were plotted. The *P* value from Student *t* test is shown on top.

3,6-dimethylamino substitution on the chromophore, 3,6-DMAD, showed the most potent and comprehensive IRE1α inhibitory activity in all cell-based and cell-free assays. These compounds also revealed a novel MOA through its disruption of IRE1α oligomerization. Finally, 3,6-DMAD demonstrated significant cytotoxicity against multiple myeloma cell lines, blocked *XBP1* splicing in XBP1-luc transgenic reporter mice, and inhibited multiple myeloma tumor xenograft growth.

The complexity of the data obtained from HTS results in large signals dominating the analysis whereas subtle and possibly more potent hits may remain undetected. In this study, we have shown that topological methods may be superior in detecting subtle but real signals from HTS data (29, 30, 33). Based upon a conventional analysis in which compounds are ranked by %inhibition of XBP1-luciferase signal, the acridine compounds were not obvious candidate for further investigation (21). The methodology from this study utilizes a network-based organization of the data so that the relatedness of promising lead compounds to other compounds in the chemical library is readily available and this information can be used for rapidly developing SAR data, resulting in a more efficient drug discovery process.

Our group first reported the feasibility of targeting IRE1α with a small molecule inhibitor, STF-083010 (21). This compound inhibited *in vitro* RNase activity of IRE1α, displayed cytotoxicity against multiple myeloma cell lines, and delayed RPMI 8226 xenograft growth. The mechanism of inhibition of STF083010

was further elucidated by a later study (23), showing that both STF-083010 and 4μ8C, a novel IRE1α RNase inhibitor, binds to K907 in the RNase domain of hIRE1α. Another XBP1s inhibitor, MKC-3946, delayed RPMI 8226 xenograft growth following a 100 mg/kg daily dose (17). Its MOA may be similar to STF083010 and 4μ8C, as MKC-3946 has the same HAA motif common to the released forms of STF083010 and 4μ8C (26). In addition, toyocamycin, an adenosine analogue, inhibits XBP1s and significantly suppressed RPMI 8226 xenograft growth with unknown MOA (24).

The mechanism of IRE1α activation during ER stress was extensively characterized. Accumulation of unfolded and misfolded proteins in the ER stimulates IRE1α trans-autophosphorylation and dimerization of its kinase and RNase domain to form the active catalytic site (3). Further analysis revealed that upon activation, IRE1α assembles into high-order oligomers, which is essential to its function (4, 37). This process was successfully visualized by detecting GFP-tagged IRE1α foci formation through live cell imaging (37). Our *in vitro* and cell-based assays revealed that a set of acridine derivatives block *XBP1* splicing with variable potency through interfering with IRE1α oligomerization as a novel MOA. 3,6-DMAD, the most potent of this class of drugs, inhibited both oligomerization and *in vitro* RNase activity of IRE1α, suggesting that substitution of the acridine chromophore induces additional activity targeting the RNase activity. Further SAR analysis to clarify the critical structural features of this chemical prototype for inhibiting *XBP1* splicing will be the subject of future studies.

In conclusion, by utilizing TDA analysis on HTS, we identified a class of acridine derivatives as potent and specific inhibitors of the IRE1α–XBP1 branch of UPR with prominent cytotoxicity on multiple myeloma cells as well as *in vivo* multiple myeloma tumor growth. Therefore, our findings have defined a class of compounds with a novel MOA and provide a strong preclinical rationale for further development of this class of compounds as a therapeutic strategy for multiple myeloma patients.

Disclosure of Potential Conflicts of Interest

M. Alagappan is a consultant/advisory board member for Ayasdi Inc. P.Y. Lum has ownership interest in Ayasdi Inc. No potential conflicts of interest were disclosed by the other authors.

Authors' Contributions

Conception and design: D. Jiang, N. Denko, A.J. Giaccia, Q.-T. Le, M. Niwa, A.C. Koong

Development of methodology: D. Jiang, A. Tam, M. Alagappan, A. Gupta, M. Niwa, A.C. Koong

Acquisition of data (provided animals, acquired and managed patients, provided facilities, etc.): D. Jiang, A. Tam, M.P. Hay, M. Kozak, D.E. Solow-Cordero, M. Niwa

Analysis and interpretation of data (e.g., statistical analysis, biostatistics, computational analysis): D. Jiang, A. Tam, M. Alagappan, D.E. Solow-Cordero, P.Y. Lum, N. Denko, A.J. Giaccia, Q.-T. Le, M. Niwa, A.C. Koong

Writing, review, and/or revision of the manuscript: D. Jiang, M. Alagappan, M.P. Hay, P.Y. Lum, N. Denko, A.J. Giaccia, Q.-T. Le, M. Niwa, A.C. Koong

Administrative, technical, or material support (i.e., reporting or organizing data, constructing databases): D. Jiang, D.E. Solow-Cordero, A.C. Koong

Study supervision: M. Niwa, A.C. Koong

Grant Support

This work was supported by grants from the NIH (P01CA067166; to Q.T. Le, N. Denko, A.J. Giaccia, A.C. Koong).

The costs of publication of this article were defrayed in part by the payment of page charges. This article must therefore be hereby marked *advertisement* in accordance with 18 U.S.C. Section 1734 solely to indicate this fact.

Received January 8, 2016; revised May 17, 2016; accepted June 7, 2016; published OnlineFirst June 15, 2016.

Reference

1. Walter P, Ron D. The unfolded protein response: from stress pathway to homeostatic regulation. Science 2011;334:1081–6.
2. Davenport EL, Moore HE, Dunlop AS, Sharp SY, Workman P, Morgan GJ, et al. Heat shock protein inhibition is associated with activation of the unfolded protein response pathway in myeloma plasma cells. Blood 2007;110:2641–9.
3. Lee KP, Dey M, Neculai D, Cao C, Dever TE, Sicheri F. Structure of the dual enzyme Ire1 reveals the basis for catalysis and regulation in nonconventional RNA splicing. Cell 2008;132:89–100.
4. Korennykh AV, Egea PF, Korostelev AA, Finer-Moore J, Zhang C, Shokat KM, et al. The unfolded protein response signals through high-order assembly of Ire1. Nature 2009;457:687–93.
5. Hetz C, Chevet E, Harding HP. Targeting the unfolded protein response in disease. Nat Rev Drug Discov 2013;12:703–19.
6. Tam AB, Koong AC, Niwa M. Ire1 has distinct catalytic mechanisms for XBP1/HAC1 splicing and RIDD. Cell Rep 2014;9:850–8.
7. Hollien J, Lin JH, Li H, Stevens N, Walter P, Weissman JS. Regulated Ire1-dependent decay of messenger RNAs in mammalian cells. J Cell Biol 2009;186:323–31.
8. Kurata M, Yamazaki Y, Kanno Y, Ishibashi S, Takahara T, Kitagawa M, et al. Anti-apoptotic function of Xbp1 as an IL-3 signaling molecule in hematopoietic cells. Cell Death Dis 2011;2:e118.
9. Shajahan AN, Riggins RB, Clarke R. The role of X-box binding protein-1 in tumorigenicity. Drug News Perspect 2009;22:241–6.
10. Davies MP, Barraclough DL, Stewart C, Joyce KA, Eccles RM, Barraclough R, et al. Expression and splicing of the unfolded protein response gene XBP-1 are significantly associated with clinical outcome of endocrine-treated breast cancer. Int J Cancer 2008;123:85–8.
11. Chen X, Iliopoulos D, Zhang Q, Tang Q, Greenblatt MB, Hatziapostolou M, et al. XBP1 promotes triple-negative breast cancer by controlling the HIF1alpha pathway. Nature 2014;508:103–7.
12. Romero-Ramirez L, Cao H, Regalado MP, Kambham N, Siemann D, Kim JJ, et al. X box-binding protein 1 regulates angiogenesis in human pancreatic adenocarcinomas. Transl Oncol 2009;2:31–8.
13. Nakamura M, Gotoh T, Okuno Y, Tatetsu H, Sonoki T, Uneda S, et al. Activation of the endoplasmic reticulum stress pathway is associated with survival of myeloma cells. Leuk Lymphoma 2006;47:531–9.
14. Carrasco DR, Sukhdeo K, Protopopova M, Sinha R, Enos M, Carrasco DE, et al. The differentiation and stress response factor XBP-1 drives multiple myeloma pathogenesis. Cancer Cell 2007;11:349–60.
15. Iwakoshi NN, Lee AH, Glimcher LH. The X-box binding protein-1 transcription factor is required for plasma cell differentiation and the unfolded protein response. Immunol Rev 2003;194:29–38.
16. Munshi NC, Hideshima T, Carrasco D, Shammas M, Auclair D, Davies F, et al. Identification of genes modulated in multiple myeloma using genetically identical twin samples. Blood 2004;103:1799–806.
17. Mimura N, Fulciniti M, Gorgun G, Tai YT, Cirstea D, Santo L, et al. Blockade of XBP1 splicing by inhibition of IRE1alpha is a promising therapeutic option in multiple myeloma. Blood 2012;119:5772–81.
18. Lee AH, Iwakoshi NN, Anderson KC, Glimcher LH. Proteasome inhibitors disrupt the unfolded protein response in myeloma cells. Proc Natl Acad Sci U S A 2003;100:9946–51.
19. Bagratuni T, Wu P, Gonzalez de Castro D, Davenport EL, Dickens NJ, Walker BA, et al. XBP1s levels are implicated in the biology and outcome of myeloma mediating different clinical outcomes to thalidomide-based treatments. Blood 2010;116:250–3.

20. Jiang D, Niwa M, Koong AC. Targeting the IRE1alpha-XBP1 branch of the unfolded protein response in human diseases. Sem Cancer Biol 2015;33: 48–56.
21. Papandreou I, Denko NC, Olson M, Van Melckebeke H, Lust S, Tam A, et al. Identification of an Ire1alpha endonuclease specific inhibitor with cytotoxic activity against human multiple myeloma. Blood 2011; 117:1311–4.
22. Volkmann K, Lucas JL, Vuga D, Wang X, Brumm D, Stiles C, et al. Potent and selective inhibitors of the inositol-requiring enzyme 1 endoribonuclease. J Biol Chem 2011;286:12743–55.
23. Cross BC, Bond PJ, Sadowski PG, Jha BK, Zak J, Goodman JM, et al. The molecular basis for selective inhibition of unconventional mRNA splicing by an IRE1-binding small molecule. Proc Natl Acad Sci U S A 2012;109: E869–78.
24. Ri M, Tashiro E, Oikawa D, Shinjo S, Tokuda M, Yokouchi Y, et al. Identification of Toyocamycin, an agent cytotoxic for multiple myeloma cells, as a potent inhibitor of ER stress-induced XBP1 mRNA splicing. Blood Cancer J 2012;2:e79.
25. Wang L, Perera BG, Hari SB, Bhhatarai B, Backes BJ, Seeliger MA, et al. Divergent allosteric control of the IRE1alpha endoribonuclease using kinase inhibitors. Nat Chem Biol 2012;8:982–9.
26. Sanches M, Duffy NM, Talukdar M, Thevakumaran N, Chiovitti D, Canny MD, et al. Structure and mechanism of action of the hydroxy-aryl-aldehyde class of IRE1 endoribonuclease inhibitors. Nat Commun 2014;5:4202.
27. Mahoney DJ, Lefebvre C, Allan K, Brun J, Sanaei CA, Baird S, et al. Virus-tumor interactome screen reveals ER stress response can reprogram resistant cancers for oncolytic virus-triggered caspase-2 cell death. Cancer Cell 2011;20:443–56.
28. Carlsson G. Topology and data. Bull American Math Soc 2009;46: 255–308.
29. Lum PY, Singh G, Lehman A, Ishkanov T, Vejdemo-Johansson M, Alagappan M, et al. Extracting insights from the shape of complex data using topology. Sci Rep 2013;3:1236.
30. Nicolau M, Levine AJ, Carlsson G. Topology based data analysis identifies a subgroup of breast cancers with a unique mutational profile and excellent survival. Proc Natl Acad Sci U S A 2011;108:7265–70.
31. Li L, Cheng WY, Glicksberg BS, Gottesman O, Tamler R, Chen R, et al. Identification of type 2 diabetes subgroups through topological analysis of patient similarity. Sci Translat Med 2015;7:311ra174.
32. Nielson JL, Paquette J, Liu AW, Guandique CF, Tovar CA, Inoue T, et al. Topological data analysis for discovery in preclinical spinal cord injury and traumatic brain injury. Nat Commun 2015;6:8581.
33. Chan JM, Carlsson G, Rabadan R. Topology of viral evolution. Proc Natl Acad Sci U S A 2013;110:18566–71.
34. Sarikonda G, Pettus J, Phatak S, Sachithanantham S, Miller JF, Wesley JD, et al. CD8 T-cell reactivity to islet antigens is unique to type 1 while CD4 T-cell reactivity exists in both type 1 and type 2 diabetes. J Autoimmun 2014;50:77–82.
35. Sidrauski C, Walter P. The transmembrane kinase Ire1p is a site-specific endonuclease that initiates mRNA splicing in the unfolded protein response. Cell 1997;90:1031–9.
36. Korennykh AV, Korostelev AA, Egea PF, Finer-Moore J, Stroud RM, Zhang C, et al. Structural and functional basis for RNA cleavage by Ire1. BMC Biol 2011;9:47.
37. Li H, Korennykh AV, Behrman SL, Walter P. Mammalian endoplasmic reticulum stress sensor IRE1 signals by dynamic clustering. Proc Natl Acad Sci U S A 2010;107:16113–8.
38. Feldman JP, Goldwasser R, Mark S, Schwarts J, Orion I. A mathematical model for tumor volume evaluation using two-dimensions. J Appl Quant Methods 2009;4:455–62.
39. Spiotto MT, Banh A, Papandreou I, Cao H, Galvez MG, Gurtner GC, et al. Imaging the unfolded protein response in primary tumors reveals microenvironments with metabolic variations that predict tumor growth. Cancer Res 2010;70:78–88.
40. Wilson WR, Thompson LH, Anderson RF, Denny WA. Hypoxia-selective antitumor agents. 2. Electronic effects of 4-substituents on the mechanisms of cytotoxicity and metabolic stability of nitracrine derivatives. J Med Chem 1989;32:31–8.
41. Siim BG, Hicks KO, Pullen SM, van Zijl PL, Denny WA, Wilson WR. Comparison of aromatic and tertiary amine N-oxides of acridine DNA intercalators as bioreductive drugs. Cytotoxicity, DNA binding, cellular uptake, and metabolism. Biochem Pharmacol 2000;60:969–78.
42. Denny WA. Dual topoisomerase I/II poisons as anticancer drugs. Expert Opin Investig Drugs 1997;6:1845–51.
43. Galdino-Pitta MR, Pitta MG, Lima MC, Galdino LS, Pitta RI. Niche for acridine derivatives in anticancer therapy. Mini Rev Med Chem 2013; 13:1256–71.
44. Arlin ZA.Current status of amsacrine (AMSA) combination chemotherapy programs in acute leukemia. Cancer Treat Rep 1983;67:967–70.
45. Dittrich C, Dieras V, Kerbrat P, Punt C, Sorio R, Caponigro F, et al. Phase II study of XR5000 (DACA), an inhibitor of topoisomerase I and II, administered as a 120-h infusion in patients with advanced ovarian cancer. Invest New Drugs 2003;21:347–52.
46. Dittrich C, Coudert B, Paz-Ares L, Caponigro F, Salzberg M, Gamucci T, et al. Phase II study of XR 5000 (DACA), an inhibitor of topoisomerase I and II, administered as a 120-h infusion in patients with non-small cell lung cancer. Eur J Cancer 2003;39:330–4.
47. Twelves C, Campone M, Coudert B, Van den Bent M, de Jonge M, Dittrich C, et al. Phase II study of XR5000 (DACA) administered as a 120-h infusion in patients with recurrent glioblastoma multiforme. Ann Oncol 2002;13:777–80.
48. Caponigro F, Dittrich C, Sorensen JB, Schellens JH, Duffaud F, Paz Ares L, et al. Phase II study of XR 5000, an inhibitor of topoisomerases I and II, in advanced colorectal cancer. Eur J Cancer 2002;38:70–4.
49. Denny WA, Baguley BC, Cain BF, Waring MJ. Antitumour acridines. In: Neidle S, Waring MJ, editors. Molecular aspects of anti-cancer drug action. London, United Kingdom: MacMillan; 1983. p. 1–34.